RSC Advances

PAPER

View Article Online
View Journal | View Issue

Cite this: *RSC Adv.*, 2026, **16**, 29576

Magnetic-field-free separation and recovery of MXene-doped GO composites *via* dye-bridged reassembly in dye adsorption

Jin Yang,[ab] Xiaoxia Yan,[ad] Yifei Qin,[ab] Dazhi Zhang,[a] Jingyi Zhao,[a] Yi Yu,[abc] Qingjun Liu *[ab] and Wenshuai Jiang *[abc]

Dye wastewater, which poses serious threats to ecosystems and human health, is very difficult to treat. Graphene oxide (GO) has significant potential for dye adsorption. However, the practical application of GO in dye wastewater treatment is hindered by its high water solubility, which prevents its efficient separation and recovery after dye adsorption. In this study, we found that doping a small amount of MXene into GO induces composite dye-bridged reassembly during dye adsorption. The reassembled composite possesses favorable stability under external forces, thus enabling solid–liquid separation and material recovery without an external magnetic field. Notably, this dye adsorption-induced reassembly phenomenon was not observed in pure GO or pure MXene dye adsorption systems. The experimental results demonstrated that a small-fragmented GO/MXene composite with 20% MXene doping achieved optimal methylene blue (MB) adsorption and dye-bridged reassembly performance, with a maximum experimental adsorption capacity measured in practice of 883.17 mg g^{-1}. The MB removal capacity of the composite was maintained over a wide pH range, with dye-bridged reassembly preferentially occurring under acidic and weakly alkaline conditions (pH 3–9). Higher dosages enhanced MB removal but impaired the dye-bridged reassembly, whereas thermal annealing reduced the composite adsorption capacity but preserved its dye-bridged reassembly ability. Although the presence of cations hindered MB adsorption, they promoted reassembly efficiency, which was positively correlated with cation valence. A quantitative recovery of approximately 95% was achieved with the GO/MXene composite. The proposed strategy enables efficient and scalable dye removal and offers a new path for high-performance and sustainable dye wastewater treatment.

Received 13th March 2026
Accepted 27th May 2026

DOI: 10.1039/d6ra02121b

rsc.li/rsc-advances

1. Introduction

Dye wastewater typically contains numerous recalcitrant organic compounds that pose serious threats to ecosystems and human health.[1,2] Current dye wastewater treatment methods include physical adsorption,[3] chemical oxidation,[4] and biodegradation.[5] Among these, adsorption is one of the most promising end-of-pipe treatment methods owing to its simplicity, low energy consumption, and easy modularization.[6]

Graphene oxide (GO) has demonstrated significant potential for dye adsorption owing to its unique two-dimensional structure, large specific surface area, and abundant oxygen-containing functional groups.[7,8] However, because of its high hydrophilicity, GO becomes dispersed as single layers in water, making solid–liquid separation extremely difficult after adsorption, which is a key bottleneck restricting its practical application.[9–12] To tackle this issue, researchers have developed various modification strategies, including fabricating GO into two-dimensional membrane materials,[13] constructing three-dimensional hydrogel structures,[14] and introducing magnetic modifications.[15–17] However, all these methods have some drawbacks: membrane separation technology faces a tradeoff between flux and adsorption capacity; hydrogel modification sacrifices the specific surface area and active adsorption sites of GO; magnetic modification not only requires an external magnetic field for assisted separation but also tends to cause secondary pollution due to the dissolution of magnetic components. Therefore, developing a facile and efficient separation and recovery technology for GO-based adsorbents holds significant research value and application prospects.

MXene ($Ti_3C_2T_x$), a new type of two-dimensional transition metal carbides/nitrides, exhibits metallic conductivity and controllable surface chemistry properties,[18–20] thus it holds

[a]School of Medical Engineering, Henan Medical University, Xinxiang, Henan 453003, People's Republic of China. E-mail: 171024@xxmu.edu.cn; qjliu@zju.edu.cn
[b]Xinxiang Key Laboratory of Neurobiosensor, Xinxiang, Henan 453003, People's Republic of China
[c]Henan Engineering Technology Research Center of Neural Sensing and Control, Henan 453003, People's Republic of China
[d]School of Digital Technology Industry, Zhengzhou Sias University, Henan 451150, People's Republic of China

potential application prospects in the field of environmental remediation. When applied to dye adsorption, MXenes can capture dye molecules through electrostatic interaction and hydrogen bonding.[21–23] According to previous reports, the incorporation of MXene into GO materials can enhance dye removal performance. Our previous work on cation-regulated methylene blue (MB) adsorption using GO and GO/MXene membranes confirmed that the introduction of a small amount of MXene can boost the dye adsorption capacity of GO.[24] Furthermore, in our investigation on dye adsorption using GO/MXene composite membranes, we observed that the fragmented GO/MXene membrane spontaneously reconnected *via* dye-bridged reassembly upon MB adsorption while maintaining favorable stability under external forces (Video S1). This process is occasionally accompanied by white flocculent connections (Fig. S1), which is distinctly different from the agglomeration behavior of GO in aqueous solutions (Video S2), thereby enabling facile separation from water bodies. Notably, this phenomenon was not observed in dye adsorption experiments using pure GO or MXene. Therefore, we hypothesize that cutting or grinding GO/MXene membrane into fragments for dye wastewater treatment can not only overcome the decline in adsorption performance caused by self-stacking during membrane fabrication but also address the critical challenge of solid–liquid separation and recovery of GO after dye adsorption through the dye-bridged reassembly behavior induced by dye adsorption.

Herein, the as-prepared GO/MXene composite was cut into fragments or ground into powder, and the dye adsorption performance and the dye adsorption-induced reassembly behavior of the composite were systematically investigated. The results demonstrated that the degree of fragmentation of the composite, MXene doping ratio, adsorbent dosage, solution pH, membrane thermal treatment temperature, and presence of different cations exerted significant effects on MB adsorption and the subsequent MB adsorption-induced reassembly. Therefore, a comprehensive balance among these factors is essential for practical applications. In addition, after identifying the macroscopic phenomena and assembly effects of dye-bridged reassembly, to further reveal its internal action mechanism, we provided a reasonable explanation for the mechanism of dye-bridged reassembly by zeta potential analysis and characterization of flocculent connections. This study demonstrates the efficient separation and recovery of GO after dye adsorption without magnetic fields, provides a novel strategy for dye wastewater treatment, and exhibits considerable scientific significance and application prospects.

2. Experimental section

2.1 Materials

Graphene oxide solution (GO, 5 mg mL^{-1}) was purchased from Angxing New Carbon Materials Co., Ltd, Ti_3C_2 (MXene, 5 mg mL^{-1}) from Beike 2D Materials Co., Ltd. Poly(vinylidene fluoride) filter membranes (PVDF, Φ 50 mm, 0.45 μm pore size) were supplied by Dalian Elite Analytical Instrument Co., Ltd. Methylene blue (MB) was purchased from Tianjin Yongda Chemical Reagent Co., Ltd, methyl orange (MO) from Shanghai Aladdin Biochemical Technology Co., Ltd. Anhydrous ethanol was obtained from Tianjin Deen Chemical Reagent Co., Ltd. Hydrochloric acid (HCl) was supplied by Zhengzhou Panye Chemical Reagent Factory, and ammonium hydroxide (NH_4OH) by Tianjin Damao Chemical Reagent Factory. Magnesium chloride ($MgCl_2$) and sodium chloride (NaCl) was purchased from Shanghai Aladdin Biochemical Technology Co., Ltd, potassium chloride (KCl) and calcium chloride anhydrous ($CaCl_2$) were purchased from Tianjin Damao Chemical Reagent Factory, and aluminum sulfate ($Al_2(SO_4)_3$) was purchased from Rhawn Chemical Reagent Co., Ltd. All chemicals were used as received without further purification. Deionised water was employed in all experiments.

2.2 Preparation of GO/MXene membranes

In this study, the GO/MXene composite membrane was fabricated using a facile drop-casting method.[25] First, the Ti_3C_2 MXene dispersion and GO solution, both at a concentration of 5 mg mL^{-1}, were mixed in a beaker in a predetermined ratio. The mixture was ultrasonicated for 30 min under magnetic stirring to achieve a homogeneous dispersion of the two components. Subsequently, a certain volume of the mixed dispersion was slowly drop-cast onto the surface of a hydrophobic PVDF substrate placed in a glass Petri dish. After drop-casting, the sample was dried in a constant-temperature oven at 50 °C for 5 h to promote tight stacking of the composite nanosheets. After cooling naturally to room temperature, the intact GO/MXene composite membrane was carefully peeled off the PVDF substrate. Thereafter, the membrane was deliberately cut into small fragments with a projected area ranging from 4.4 $\times$ 10^3 to 8.6 $\times$ 10^4 μm^2. The resulting fragmented GO/MXene composite was used for the subsequent characterization and adsorption experiments.

2.3 Characterisation

The surface morphology of the prepared materials were investigated using scanning electron microscope (SEM, Hitachi Regulus8220). The elements in the samples and their distributions were analysed using energy-dispersive spectrometer (EDS, Bruker XFlash 6160). The crystalline structures of the samples were identified using X-ray diffraction (XRD, Empyrean). The functional groups on the GO/MXene composite membranes were analysed using Fourier transform infrared (FTIR) spectrometer (Nicolet iS5). X-ray photoelectron spectroscopy (XPS) was performed using a Thermo Fisher K-alpha spectrometer (K-Alpha, USA). Contact angle measurements were performed using a contact-angle goniometer (V5).

2.4 Adsorption and dye-bridged reassembly behaviour experiments

The adsorption performance and dye-bridged reassembly behaviour of the GO/MXene composites were investigated using MB as a dye pollutant. The specific experimental steps were as follows: the cut pieces of the GO/MXene composites were placed in a glass vial containing 20 mL of MB solution (400 mg L^{-1}).

After 48 h of adsorption at 30 °C, the supernatant was collected, and the concentration of the remaining MB solution was measured at $\lambda_{max} = 665$ nm using a UV-vis spectrophotometer (TU-1810). The MB removal rate was calculated as follows (eqn (1)):

$$R = \frac{C_0 - C_t}{C_0} \times 100\% \quad (1)$$

where C_0 (mg L^{-1}) is the initial MB concentration, C_t (mg L^{-1}) is the MB concentration at different time points, and R (%) is the adsorption efficiency.

The influence of multiple factors on the dye-bridged reassembly behavior was systematically examined to investigate the dye-bridged reassembly properties of the membrane fragments induced by dye adsorption. After adsorption, the mechanically fractured GO/MXene composite spontaneously reconnected under static conditions to form flocs and achieve a stable structure. Its structural stability was investigated by ultrasonic treatment at 50 Hz. Based on this, single-factor experiments were conducted to analyze the influence of each factor on the dye-bridged reassembly efficiency and stability. The factors examined include the membrane fragment size, MXene content, membrane dosage, solution pH, membrane heat treatment temperature, presence of different cations, and dye type.

2.5 Isotherm model

Adsorption isotherms are commonly used to describe the equilibrium distribution of adsorbed molecules between liquid and solid phases, reflecting the relationship between the pollutant concentration in the solution and the adsorption capacity of the adsorbent. The Langmuir (eqn (2)) and the Freundlich (eqn (3)) adsorption isotherms were used to investigate the experimental results.

$$Q_e = \frac{Q_m K_L C_e}{1 + K_L C_e} \quad (2)$$

$$Q_e = K_F \times C_e^{\frac{1}{n}} \quad (3)$$

where Q_m and Q_e are the maximum and equilibrium capacity of MB, respectively; C_e (mg L^{-1}) is the concentration of MB at adsorption equilibrium; K_L (L mg^{-1}) represents the Langmuir isotherm constant; and K_F ((L $mg^{-1})^{1/n}$ mg g^{-1}) and n represent the Freundlich constants, corresponding to the adsorption capacity and adsorption intensity, respectively.

2.6 Kinetic model

To investigate adsorption kinetics, both pseudo-first-order (eqn (4)) and pseudo-second-order (eqn (5)) kinetic models were used to simulate the adsorption process.

$$Q_t = Q_e(1 - e^{-k_1 t}) \quad (4)$$

$$Q_t = \frac{Q_e^2 k_2 t}{1 + k_2 Q_e t} \quad (5)$$

where Q_t (mg g^{-1}) and Q_e (mg g^{-1}) are the adsorption capacity of MB at time t (h) and at adsorption equilibrium, respectively, and k_1 (h^{-1}) and k_2 (g (mg^{-1} h^{-1})) are the rate constants for the pseudo-first-order and pseudo-second-order models, respectively.

To further explain the adsorption mechanism and identify the steps controlling the adsorption rate, the potential effect of the particle diffusion resistance on the adsorption process was analyzed using the kinetic model developed by Weber and Morris[26] (eqn (6)).

$$Q_t = K_i t^{1/2} + C_i \quad (6)$$

where K_i (mg g^{-1} $h^{-0.5}$) is the rate constant of intraparticle diffusion, and C_i (mg g^{-1}) is the intercept, which is related to the thickness of the adsorption boundary layer.

3. Results and discussion

3.1 Characterisation of GO/MXene

Fig. 1 illustrates the preparation process of the GO/MXene composite, along with its MB adsorption performance and dye-bridged reassembly behavior. As shown in the flowchart, a homogeneous dispersion of GO and Ti_3C_2 MXene was uniformly drop-casting onto a PVDF substrate using a facile drop-casting method. Finally, a compact GO/MXene composite membrane was formed by drying and stacking the nanosheet. After the membrane was fully formed and cooled to room temperature, it was carefully peeled from the PVDF substrate and deliberately cut into membrane fragments of a certain size range for the subsequent experiments. This method enables the directional arrangement of nanosheets during solvent evaporation, wherein the two-dimensional sheet structure of GO interweaves with the layered structure of MXene to form a dense membrane with abundant interlayer channels. This structure provides favorable conditions for the diffusion and adsorption of MB molecules. Manual cutting can yield membrane fragments with good uniformity, which guarantees the consistency of conditions in subsequent characterization and adsorption tests. This fragmentation process significantly increased the specific surface area and number of available active sites, thereby enhancing the adsorption rate. After a period of time following the completion of MB adsorption, the composite particles spontaneously undergo dye-bridged reassembly *via* intermolecular interactions, forming a membrane-like structure interconnected by flocculent networks.

The SEM characterization results in Fig. 2 clearly reveal the microstructural differences between the pure GO membrane and the GO/MXene composite membrane. Compared with the pure GO membrane (Fig. 2a and c), the surface of the GO/MXene composite (Fig. 2b) exhibits dense and irregular wrinkled structures with significantly increased roughness. From a cross-sectional view, the GO/MXene composite (Fig. 2d) shows a looser layered stacking feature, which not only considerably increases the specific surface area of the membrane but also provides more active sites for the subsequent adsorption process.[27] Furthermore, the EDS spectra in Fig. 2e–h illustrate

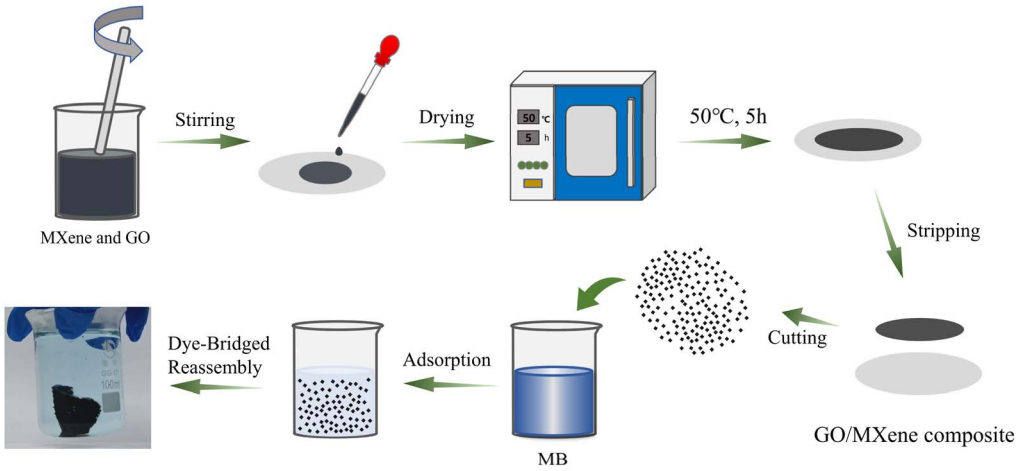

Fig. 1 The preparation of GO/MXene composites and the dye-bridged reassembly behavior after MB adsorption.

the presence of elements such as C, O, F, and Ti within the GO/MXene composite, providing evidence of the elemental composition and distribution.[28,29]

As shown in the XRD patterns in Fig. 3a, the introduction of MXene causes a leftward shift in 2θ, further confirming that MXene increases the interlayer spacing of GO. FTIR spectroscopy was used to analyze the chemical composition of the membrane.[30] Fig. 3b shows the spectra of the GO, MXene, and GO/MXene membranes before and after MB adsorption. The GO/MXene composite retained the characteristic signals of both

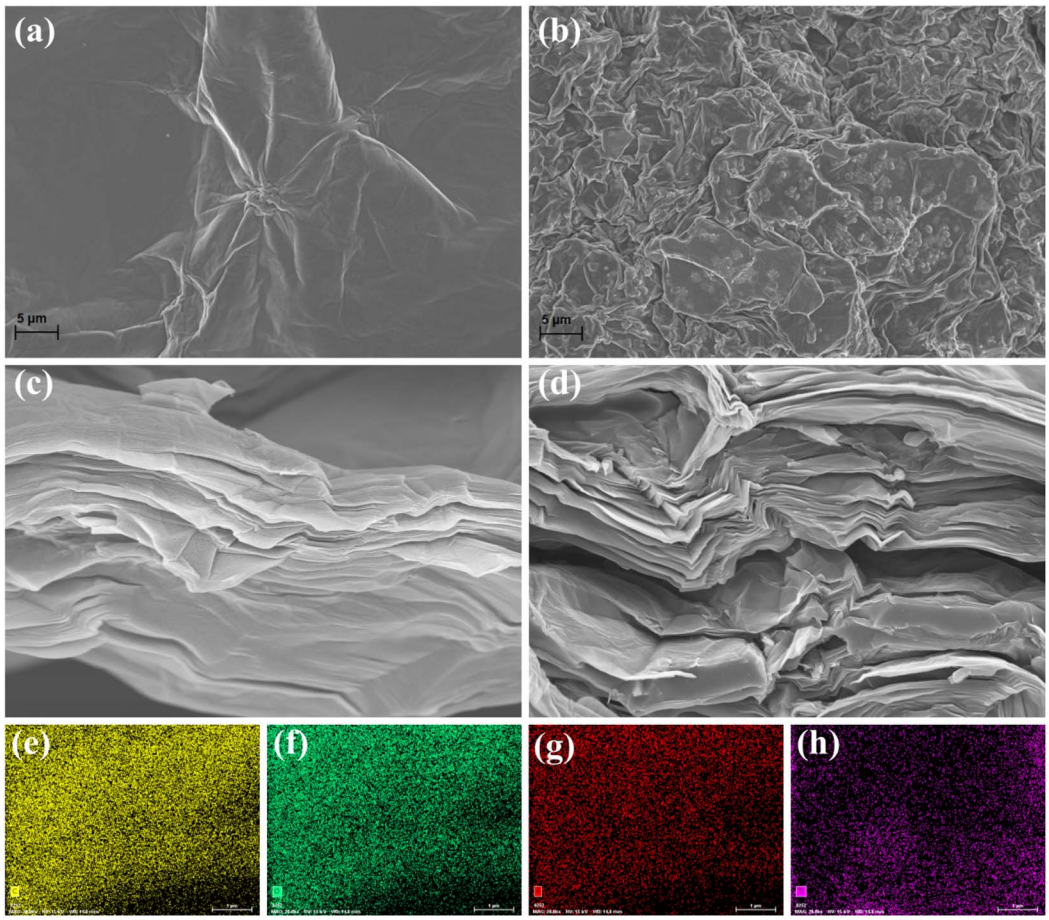

Fig. 2 SEM results of GO and GO/MXene membranes: (a and b) surface view and (c and d) cross-sectional view, (e–h) EDS spectra of the GO/MXene composite.

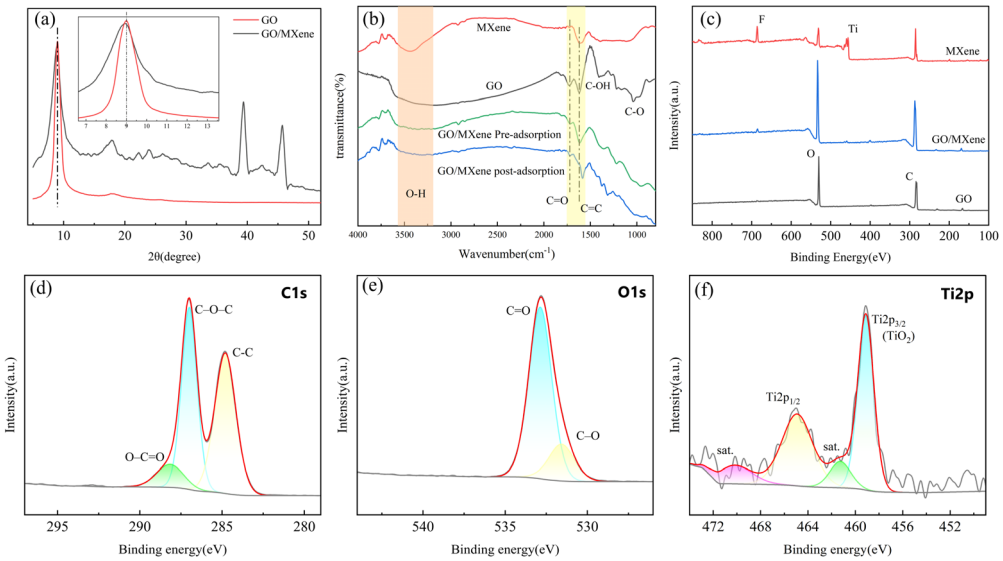

Fig. 3 (a) XRD patterns of GO and GO/MXene membranes. (b) FTIR spectra of GO, MXene, and GO/MXene membranes before and after MB adsorption. (c) XPS spectra of GO, MXene, and GO/MXene membranes; (d–f) XPS high-resolution spectra of GO/MXene membrane at C 1s, O 1s, and Ti 2p core levels.

GO and MXene, confirming that MXene was successfully incorporated into GO. The broad absorption band at approximately 3400 cm^{-1} was attributed to the O–H stretching vibration, whereas the narrower peak found in MXene was ascribed to surface –OH/–F terminal groups. A weak peak at 2920 cm^{-1} was assigned to C–H stretching, whereas the sharp band at 1721 cm^{-1} was associated with the C=O stretching vibration. After MB adsorption, the intensity of the C=O peak decreased markedly, indicating that the carbonyl groups participated in pollutant capture *via* coordination or electrostatic interactions. The peaks at 1615, 1406, and 1040 cm^{-1} were assigned to the C=C skeletal vibrations, O–H bending in alcoholic hydroxyls, and C–O stretching from epoxy or ether groups, respectively. Notably, the intensity of the ~3400 cm^{-1} hydroxyl band diminished after adsorption, accompanied by a weakened C=O peak, suggesting that the –OH and C=O groups in the composite served as primary adsorption sites, forming hydrogen or coordination bonds with dye molecules, whereas the terminal hydroxyls in MXene contributed synergistically. Additionally, the C=C stretching band shifted after adsorption, indicating the formation of π–π stacking between dye molecules and the GO/MXene composite.

XPS was used to analyze the GO, GO/MXene, and MXene membranes. As shown in Fig. 3c, the survey scan suggests that Ti and F are present in the GO/MXene membrane, indicating that MXene was introduced into the GO/MXene membrane. In the high-resolution C 1s spectrum (Fig. 3d), peaks at 288.16, 286.99, and 284.8 eV were attributed to C–C=O, C–O–C and C–C bonds, respectively. The high-resolution O 1s spectrum (Fig. 3e) exhibited peaks at 532.87 and 531.57 eV, corresponding to C=O and C–O bonds, respectively. The high-resolution Ti 2p spectrum (Fig. 3f) showed peaks at 464.92 and 459.11 eV, corresponding to Ti $2p_{1/2}$ and Ti $2p_{3/2}$, respectively, and the peaks at 470.16 and 461.28 eV were identified as satellite peaks.

3.2 Dye adsorption and dye-adsorption-driven dye-bridged reassembly of GO/MXene composite

Fig. 4 shows the comparison of the dye adsorption performance and dye-bridged reassembly behavior of the GO/MXene composite. Specifically, 20 mg of MXene fragments, GO fragments, and GO/MXene composite fragments were placed in 20 mL glass vials, followed by the addition of 20 mL of 400 mg L^{-1} MB solution. An additional GO/MXene composite fragment sample was immersed in an equal volume of pure water (without MB) as a blank control. As shown in Fig. 4a, compared with GO, the incorporation of MXene enhanced the dye adsorption rate. Contact-angle measurements revealed that the GO membrane and the GO/MXene composite membrane exhibited contact angles of 42.7° and 63.5°, respectively, confirming that favourable hydrophilicity was retained upon MXene incorporation.[31] The MB adsorption performances of intact membranes under various conditions are presented in Fig. S2. Further comparisons between the intact membranes and identically weighted, cut membranes revealed that the shredded GO/MXene composite membranes exhibited a pronounced increase in MB removal efficiency, which was ascribed to the exposure of additional active adsorption sites through fragmentation (Fig. 4b). The UV-vis spectra recorded during adsorption (Fig. 4c) corroborated this conclusion, in which the decay of the 665 nm peak intensity was markedly accelerated for the shredded membranes relative to their intact counterparts. Surprisingly, Fig. 4d shows that only the GO/MXene composite manifests a conspicuous "dye-bridged reassembly" behavior after MB adsorption, whereas no such behaviour is observed for GO or MXene membranes alone, or for GO/MXene membranes immersed in deionized water. This observation suggests that the synergistic interaction between the dye molecules and MXene can induce structural or

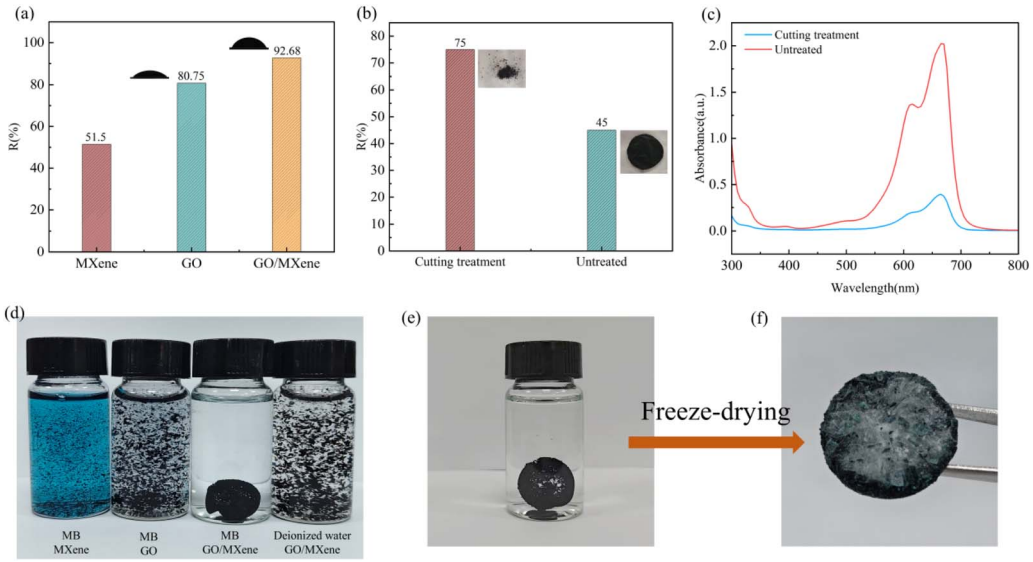

Fig. 4 (a) Dye-removal efficiencies and water-contact angles of different membranes; (b) MB removal efficiency and (c) UV-vis spectra of the adsorption solutions using intact and cut GO/MXene membranes; (d) comparison of dye-bridged reassembly behaviors among different composite materials; (e) dye-bridged reassembly behavior of GO/MXene composite and (f) its freeze-drying treatment.

interfacial reconstruction at the microscopic level, thereby providing the required conditions for membrane dye-bridged reassembly. Fig. 4e clearly shows the macroscopic membrane-like dye-bridged reassembly formed by the GO/MXene composite membrane after the adsorption of MB. Fig. 4f shows the macroscopic dye-bridged reassembly after freeze-drying, with its membrane-like morphology well preserved without obvious collapse or fragmentation. Moreover, the GO/MXene composite maintained an excellent structural stability during the recovery process, achieving a high material recovery ratio of approximately 95%.

3.3 Adsorption isotherm and kinetics

Fig. 5a shows the adsorption isotherms of the fragmented GO/MXene composite, and the results were fitted using the Langmuir and Freundlich isotherm equations. Table 1 summarizes the isotherm model constants and correlation coefficients for the adsorption of MB onto fragmented GO/MXene composites. The adsorption isotherms, kinetics, and ion diffusion models of the intact GO/MXene membranes are shown in Fig. S3, and the corresponding correlation coefficients are listed in Tables S1–S3.

Table 1 lists the fitting parameters for the Langmuir and Freundlich isotherm models. The Freundlich model presents a much higher correlation coefficient ($R^2 = 0.992$) and fits the experimental data far better than the Langmuir model ($R^2 = 0.96$). Accordingly, the adsorption of MB onto the GO/MXene composites follows the Freundlich model, which indicating multilayer adsorption on a heterogeneous material surface. The adsorption capacity of the composite measured in practice was 883.17 mg g^{-1} (at 72 h), and the adsorption performance of the GO/MXene composite was compared with that of previously reported adsorbents (Table 2).

Fig. 5b and Table 3 present the kinetic fitting results for the GO/MXene composite. The pseudo-second-order model ($R_2{}^2 = 0.999$) fits the adsorption kinetics better. The relatively low k_2 value indicates slow adsorption kinetics, which is attributed to the complex surface morphology of the GO/MXene composite. These results suggest that the adsorption of MB on the GO/MXene composite is mainly governed by chemisorption and is

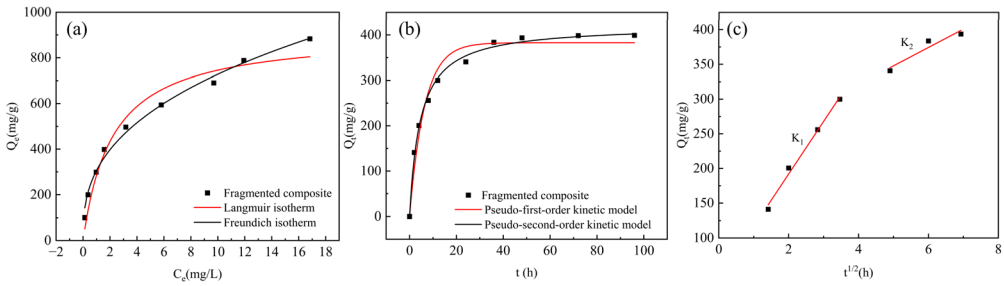

Fig. 5 Fragmented composite. (a) Langmuir and Freundlich adsorption isotherms, (b) pseudo-first-order and pseudo-second-order kinetic models (c) intraparticle diffusion model.

Table 1 Fitting parameters of the Langmuir and Freundlich models for the fragmented composite

Langmuir			Freundlich		
Q_m (mg g^{-1})	K_L (L mg^{-1})	R^2	$1/n$	K_F ((L mg^{-1})$^{1/n}$ mg g^{-1})	R^2
909.002	0.456	0.96	0.37	306.23	0.992

Table 3 Kinetics parameters for the adsorption of MB on the fragmented GO/MXene composite

Pseudo-first-order model			Pseudo-second-order model		
k_1 (h^{-1})	Q_{e1} (mg g^{-1})	R_1^2	k_2 (g (mg^{-1} h^{-1}))	Q_{e2} (mg g^{-1})	R_2^2
0.156	382.81	0.971	0.0005	421.4	0.995

accompanied by ion exchange or electron sharing.[37] The fitting results in Fig. 5c suggest that the MB adsorption on the GO/MXene composite involves two successive stages. Moreover, none of the linear relationships passed through the origin, as presented in Fig. 5c and Table 4, and the linear correlation coefficients were all greater than 0.9.

3.4 Adsorption and dye-bridged reassembly behaviors

3.4.1 Fragmentation degree. To evaluate the influence of fragmentation degree on the dye-bridged reassembly behavior, the GO/MXene composite was prepared in three size regimes: small fragments (projected area = 4.4×10^3 to 8.6×10^4 μm^2), medium fragments (8×10^6 to 1.5×10^7 μm^2), and large fragments (8.1×10^7 to 1×10^8 μm^2). All experiments were conducted in 20 mL of 400 mg L^{-1} MB solution. The small fragments exhibited the highest MB removal efficiency (Fig. 6a), and after standing for a certain period, a distinct macroscopic dye-bridged reassembly phenomenon was observed (as shown in Fig. 6b). The adjacent fragments gradually approached each other and spontaneously coalesced into stable flocs. This mechanism can be explained as follows: smaller fragmentation increases the number of active sites and provides a sufficient and tightly bound contact interface for adjacent fragments, thereby fulfilling the necessary conditions for dye-bridged reassembly. At the same volume, as the degree of fragmentation decreases, both the adsorption rate and dye-bridged reassembly efficiency decrease. Although medium and large fragments exhibit some aggregation under external disturbances, the limited effective contact area results in loose and fragile connections that cannot form a structurally continuous block. These findings demonstrate that fragment size is the key parameter regulating the dye-bridged reassembly ability of the GO/MXene composite membrane, and a small size and sufficient contact area are prerequisites for successful dye-bridged reassembly.

3.4.2 MXene doping ratio. To investigate the influence of MXene doping ratios on the "dye-bridged reassembly" behavior of GO/MXene composites, GO/MXene composites with MXene mass fractions of 10%, 20%, 40%, and 60% were prepared and tested under the same experimental conditions (20 mL, 400 mg L^{-1} MB solution). As shown in Fig. 6c and d, all the fragmented composites achieved macroscopic dye-bridged reassembly after adsorbing MB and the composite with 20% MXene performed best in terms of the MB removal rate and dye-bridged reassembly synergistic effect. Fig. S4 shows the MB adsorption by the intact membrane prepared with different MXene ratios, which also confirms that the sample with a 20% doping ratio exhibits a superior adsorption effect. Fig. S5 presents SEM images of the intact GO/MXene membranes fabricated with varying MXene ratios. The flexibility analysis of the intact membranes is presented in Fig. 6e–i, which suggests that the flexibility was maintained at a 20% MXene doping level. However, when the MXene content was further increased, the excess MXene increased the layer rigidity and stacking densification, resulting in a simultaneous reduction in the effective adsorption sites and contact area.[38] In addition, the charge shielding effect caused by the high conductivity of the MXene network may weaken the electrostatic-π synergy, ultimately leading to a synchronous decrease in the adsorption rate and dye-bridged reassembly efficiency.[39]

3.4.3 Composite dosage. To investigate the effect of composite dosage on the dye-bridged reassembly performance, 10, 20, 30, and 40 mg of the GO/MXene composite were added to 20 mL of 400 mg L^{-1} MB solution for the adsorption test. As shown in Fig. 7a, the MB removal rate increased monotonically from 62% to 96% as the dosage increased from 10 to 40 mg, mainly because of the increase in the number of adsorption sites and the effective contact area. Fig. 7b shows that dye-bridged reassembly occurred at all dosages; however, the degree of dye-bridged reassembly decreased significantly with increasing dosage. This phenomenon can be explained as

Table 2 Comparison of adsorption and separation behaviors between GO/MXene composite and other reported adsorbents

Adsorbent	Q_m (mg g^{-1})	Equilibrium time (h)	Working concentration range (mg L^{-1})	Separation method	Ref.
GO/MXene composite	883.17	72	100–900	Filtration	This work
MOF-199@AFGO/CS	412	24	50–300	Filtration	32
GO–LCTS	402.6	24	32–320	Centrifugation	33
AA-alk-MXene	193.92	48	70–90	Centrifugation	34
$Ti_3C_2T_x$/SA beads	92.17	6	40–160	Centrifugation	35
MXene/RGO foam	1099.5	60	200–1100	Filtration	27
Fe_3O_4/GO	306.5	6	50–150	Magnetic field	36

Table 4 Parameters of the intraparticle diffusion model of the fragmented composite

Stage I			Stage II		
K_1 (mg g^{-1} h$^{-0.5}$)	C_1 (mg g^{-1})	R_1^2	K_2 (mg g^{-1} h$^{-0.5}$)	C_2 (mg g^{-1})	R_2^2
75.95	40.1	0.99	26.51	215.11	0.914

follows: at a low dosage (*e.g.*, 10 mg), the number of MB molecules adsorbed per unit mass of the composite was high, leading to local adsorption site saturation and a strong driving force for dye-bridged reassembly. Conversely, an increase in the dosage reduced the adsorption load per unit mass, resulting in fewer MB molecules at each site and a weaker dye-bridged reassembly driving force. Consequently, the degree of dye-bridged reassembly decreased with increasing dosage.

3.4.4 pH condition. The pH of the solution regulates the ionization of GO, MXene, and MB, which in turn significantly affects the adsorption process.[37] Thus, the effect of the initial pH of the solution on MB removal was investigated. Experiments were conducted at pH value of 3, 5, 7, 9, and 11, as well as under unadjusted conditions (initial pH = 5.38). Fig. 8a shows that the GO/MXene composite exhibits good MB removal performance under acidic, neutral, and alkaline conditions. However, the dye-bridged reassembly process is highly sensitive to pH (Fig. 8b), occurring primarily under acidic and weakly alkaline conditions, with a more pronounced effect under acidic conditions. By contrast, under strongly alkaline conditions (pH = 11), dye-bridged reassembly was almost undetectable.

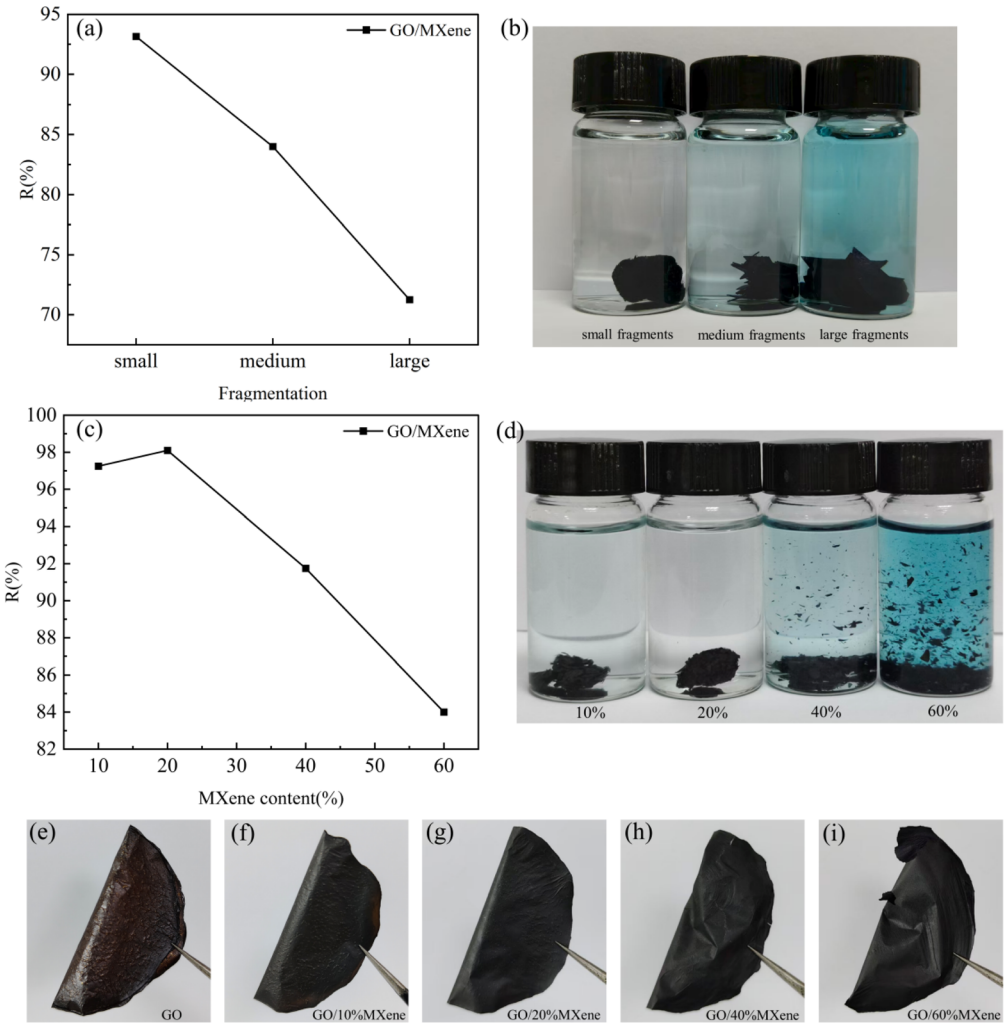

Fig. 6 (a) MB removal efficiency and (b) dye-bridged reassembly behavior of GO/MXene membranes with different fragmentation degrees. (c) MB removal efficiency and (d) dye-bridged reassembly behavior of GO/MXene fragmentation membranes under different MXene doping ratios. (e–i) Flexibility comparison of membranes.

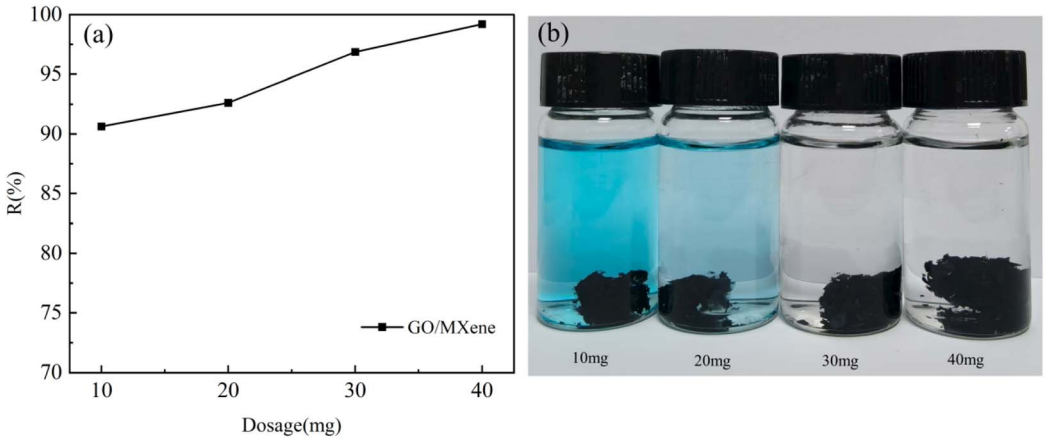

Fig. 7 (a) MB removal efficiency and (b) dye-bridged reassembly behavior of GO/MXene membranes under different composite dosages.

3.4.5 Membrane thermal treatment temperature. Thermal annealing can alter the structure and properties of GO, thereby affecting its MB adsorption performance towards MB.[40,41] To further investigate the impact of thermal treatment temperature on the dye-bridged reassembly performance of the GO/MXene composite, adsorption and dye-bridged reassembly experiments were conducted using composites heat-treated at various annealing temperatures (50, 100, 150, 175, and 200 °C). As shown in Fig. 8c, as the annealing temperature increased, the MB adsorption rate gradually decreased. When the annealing temperature exceeded 150 °C, the composite membrane nearly completely lost its ability to adsorb MB molecules, indicating that the thermal treatment temperature significantly affects the adsorption performance of the GO/MXene composite. High-temperature treatment may change the microstructure of the composite, reducing the activity of the adsorption sites and thereby weakening its adsorption capacity.[42] However, the dye-bridged reassembly ability of the GO/MXene composite was retained even after high-temperature annealing (Fig. 8d).

3.5 Dye-bridged reassembly mechanism

This study investigated the mechanism underlying the dye-bridged reassembly of the GO/MXene composite during MB adsorption. The experimental results indicated that the GO/MXene composite exhibited no dye-bridged reassembly behavior prior to MB adsorption; distinct dye-bridged reassembly occurred only after the MB molecules were adsorbed. Specifically, the dispersed composite layers combine to form stable flocs along with flocculent substances. As shown in Fig. S6, the XPS results confirmed the presence of both GO/

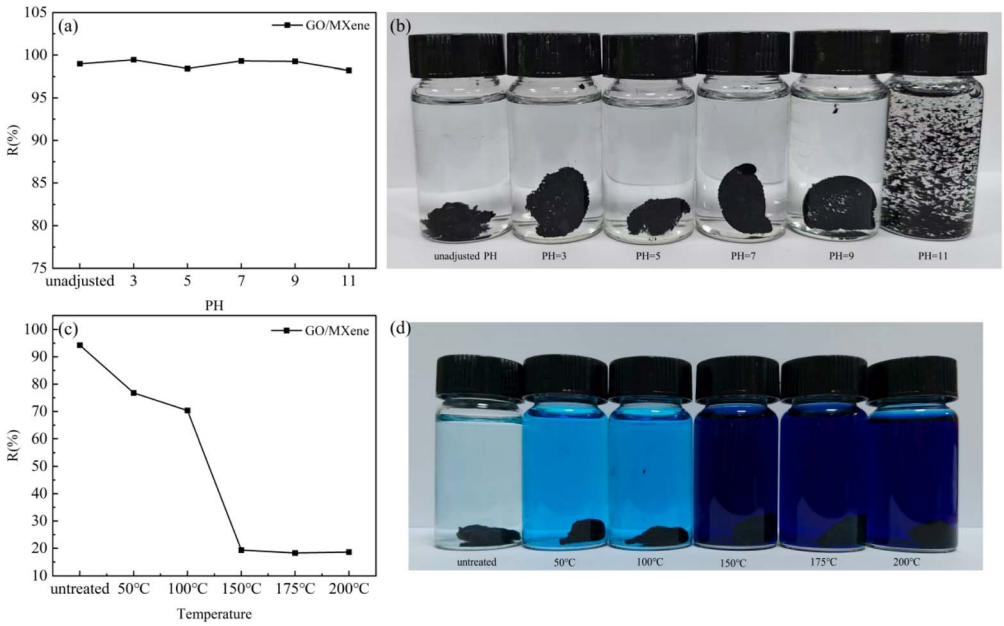

Fig. 8 (a) MB removal efficiency and (b) dye-bridged reassembly behavior of GO/MXene composite under different pH conditions. (c) MB removal efficiency and (d) dye-bridged reassembly behaviors of GO/MXene composite treated at different annealing temperatures.

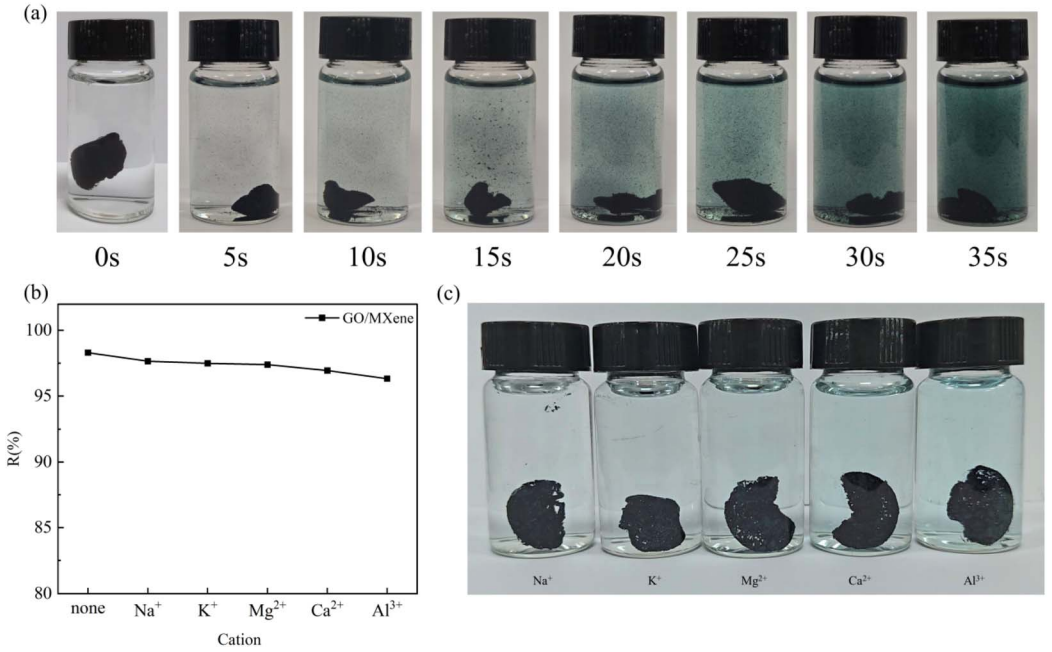

Fig. 9 (a) Structural stability of the dye-bridged reassembly the GO/MXene composite under continuous ultrasonication. (b) MB removal efficiency and (c) dye-bridged reassembly behaviours of the GO/MXene composite after incorporation of different cations.

MXene fragments and MB molecules in the flocculent connections. By contrast, neither GO nor MXene exhibited dye-bridged reassembly under identical experimental conditions. The mechanism of this phenomenon can be explained by the zeta potential analysis (Fig. S7): as a derivative of graphene, GO is rich in negatively charged oxygen-containing functional groups on its basal plane and edges. These functional groups cause electrostatic repulsion between the GO sheets when MB is not adsorbed, thus maintaining their dispersed state.[43] When the GO/MXene composite adsorbs MB, the positively charged MB molecules are electrostatically attracted to the negatively charged GO.[44] The zeta potential shows that the absolute value of the negative surface potential decreases compared with that in deionized water, which demonstrates that the adsorbed MB molecules neutralize part of the negative charge on the material surface. Simultaneously, charges can be transferred and redistributed through the MXene sheets because of their good electrical conductivity. This charge transfer further promotes electrostatic attraction, weakening the original repulsive force between the GO sheets. Combined with π–π stacking between the aromatic cores of MB and the graphitic domains of GO/MXene, a net attractive force emerges to drive dye-bridged reassembly and floc formation. Moreover, the zeta potential variation under different pH conditions further explains the pH dependence of the reassembly behaviour. An appropriately acidic environment reduces the negative surface charge density

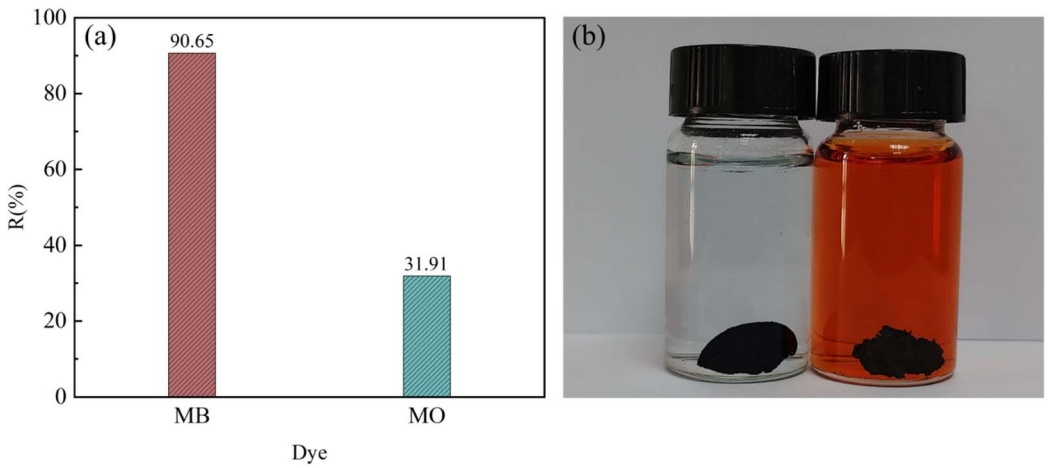

Fig. 10 (a) Dye removal efficiency and (b) dye-bridged reassembly behaviors of the GO/MXene composite using different dyes.

of the composite, which is conducive to electrostatic combination and reassembly. In addition, the spatial and temporal interactions between fragments have a significant impact on dye-bridged reassembly. Electrostatic attraction and charge transfer occur effectively only when the distance between the GO/MXene composite fragments is sufficiently small. If the fragments are too far apart, the electrostatic force is insufficient to overcome other dispersive forces (such as the solvent-induced dispersion), thereby preventing the dye-bridged reassembly. Contact time is another key factor. When the contact time is excessively short, electrostatic attraction and charging cannot proceed completely, and no dye-bridged reassembly occurs. These processes can be completed with sufficient contact time, leading to dye-bridged reassembly.

3.6 Stability

To evaluate the structural stability of the GO/MXene composite after dye-bridged reassembly, the reassembled structure was subjected to continuous ultrasonication at a frequency of 50 Hz. As shown in Video S1, the composite maintained its complete structure even under shaking conditions. As shown in Fig. 9a, the floc maintained its complete structure during the initial stage (0 s). After 5 s of ultrasonication, a small amount of debris was observed in the solution. As the ultrasonic time extended, the debris gradually increased, the reassembled structure gradually disintegrated, the previously adsorbed MB was re-released, and the color of the solution changed from light to dark. Notably, even after 35 s of continuous ultrasonication, some flocs retained their connected state, indicating good stability under dynamic disturbances.

3.7 Effect of cations

To investigate the effect of cations on the dye-bridged reassembly of the GO/MXene composite in aqueous environments, the as-prepared GO/MXene composites were immersed in MB solutions incorporated with 300 μL of 1 mol L^{-1} cation solutions (Na^+, K^+, Mg^{2+}, Ca^{2+}, Al^{3+}), with a cation-free blank control group set in parallel. As shown in Fig. 9b, the presence of cations hindered dye adsorption, and the dye removal efficiency of the composite exhibits a gradually decreased with the introduction of Na^+, K^+, Mg^{2+}, Ca^{2+}, and Al^{3+}. Among these systems, the lowest removal efficiency was observed in the presence of Al^{3+}, although it remained above 95%. By contrast, the results in Fig. 9c indicate that the incorporation of different cations significantly enhances the dye-bridged reassembly behavior of the GO/MXene composite, with a clear positive correlation between cation valence and dye-bridged reassembly efficacy. This phenomenon can be attributed to the charge regulation mechanism; the introduction of cations increases the positive charge in the solution, facilitating the neutralization of negative charges on the composite surface. As the cation valence increases, the charge neutralization effect is further strengthened. The zeta potential analysis in Fig. S8 confirms this point; with an increase in cation valence, the absolute value of the negative zeta potential gradually decreases. This leads to a significant reduction in the electrostatic repulsion between the nanosheets and a corresponding enhancement in the electrostatic attraction, thereby driving the formation of more robust reassembled structures.

3.8 Different dyes

Inspired by the dye-bridged reassembly of the GO/MXene composite induced by MB, we investigated its performance for methyl orange (MO) (operating pH = 5.85). As shown in Fig. 10a, the removal rate of MO by GO/MXene within 48 h was approximately 30%, which was lower than that of MB. A comparative analysis of the dye-bridged reassembly (Fig. 10b) shows that the MO solution can also induce aggregation of the GO/MXene composite fragments. Unlike the MB system, the anionic MO failed to neutralize the negative surface charge of GO/MXene, and a prominent electrostatic repulsion existed between the negatively charged MO molecules and the composite material. No flocculent network that could strengthen the overall structure was observed in the freeze-dried MO-assembled samples. This indicates that MO only achieves weak aggregation of composite fragments relying on π–π stacking and intermolecular hydrogen bonding. This further demonstrates that electrostatic charge neutralization dominates the superior structural stability of MB-induced dye-bridged reassembly, whereas MO merely drives limited fragment aggregation through weak intermolecular interactions.

4. Conclusions

In this study, a GO/MXene composite was employed as the core adsorbent to construct an "adsorption–reassembly–separation" system. The dye wastewater treatment performance and adsorption-induced reassembly characteristics of the composite were systematically investigated. The GO/MXene composite enabled efficient solid–liquid separation without external field assistance or centrifugation. This study provides novel insights into the practical application of GO-based materials for water treatment. Kinetic analysis revealed that the adsorption process followed a pseudo-second-order kinetic model. The GO/MXene composite exhibited an excellent dye capture capacity, and its adsorption efficiency increased significantly with higher material fragmentation. Notably, the dye-bridged reassembly of the GO/MXene composite was not observed in single GO or MXene systems. The dye-bridged reassembly behavior was more pronounced at high MB contents and weak acidity, and it persisted after thermal treatment of composite membrane. Notably, the presence of cations in the solution could promote the dye-bridged reassembly, and the structure exhibited satisfactory stability. In summary, the proposed GO/MXene-based dye wastewater treatment method features high adsorption capacity and easy separation. This offers a new route for dye wastewater purification and provides a design concept for composite adsorbents with both adsorption and self-separation properties, with significant scientific value and broad practical prospects. Future research will focus on further exploring the microscopic mechanism of dye-bridged reassembly behavior and extending relevant research to other dyes.

Author contributions

Jin Yang: writing – original draft, writing – review and editing, data curation. Xiaoxia Yan: writing – original draft, writing – review and editing, data curation. Yifei Qin: data curation. Dazhi Zhang: data curation. Jingyi Zhao: data curation. Yi Yu: methodology, formal analysis. Qingjun Liu: methodology, formal analysis, funding acquisition. Wenshuai Jiang: writing – original draft, writing – review and editing, conceptualization, methodology, formal analysis, funding acquisition.

Conflicts of interest

The authors declare that they have no known competing financial interests or personal relationships that could have appeared to influence the work reported in this paper.

Data availability

All data included in this study are available upon request by contact with the corresponding author.

Supplementary information (SI) is available. See DOI: https://doi.org/10.1039/d6ra02121b.

Acknowledgements

This work was supported by the Science and Technology Research Project of Henan Province (252102230046), the Key Scientific Research Items of Henan Province Colleges and Universities (26B416004), the Research Initiation Program for Specially Appointed Professors of Henan Medical University (505526) and the Graduate Research and Innovation Support Program of Henan Medical University (YJSCX202513Z).

References

1 A. Tkaczyk, K. Mitrowska and A. Posyniak, *Sci. Total Environ.*, 2020, **717**, 137222.
2 H. Chen, X. Yu, X. Wang, Y. He, C. Zhang, G. Xue, Z. Liu, H. Lao, H. Song and W. Chen, *J. Cleaner Prod.*, 2021, **326**, 129353.
3 A. M. Awad, S. M. Shaikh, R. Jalab, M. H. Gulied, M. S. Nasser, A. Benamor and S. Adham, *Sep. Purif. Technol.*, 2019, **228**, 115719.
4 A. Ahmadi, M. Hajilou, S. Zavari and S. Yaghmaei, *J. Cleaner Prod.*, 2023, **382**, 134967.
5 M. Almaguer, R. Carpio, T. Alves and J. Bassin, *J. Environ. Chem. Eng.*, 2018, **6**, 610–615.
6 J. E. Aguiar, J. A. Cecilia, P. A. S. Tavares, D. C. S. Azevedo, E. R. Castellón, S. M. P. Lucena and I. J. Silva, *Appl. Clay Sci.*, 2017, **135**, 35–44.
7 A. R. B. Bayantong, Y.-J. Shih, D. C. Ong, R. R. M. Abarca, C.-D. Dong and M. D. G. de Luna, *Chemosphere*, 2021, **274**, 129518.
8 P. Zhao, M. Jian, Q. Zhang, R. Xu, R. Liu, X. Zhang and H. Liu, *J. Mater. Chem. A*, 2019, **7**, 16598–16621.
9 Y. Zhao, Y. Liu, X. Zhang and W. Liao, *Chemosphere*, 2021, **262**, 127885.
10 J. Sun, C. Hu, Z. Liu, H. Liu and J. Qu, *Carbon*, 2019, **145**, 140–148.
11 X. Chen, V. Boffa, E. Gaggero, F. Meng, R. Navone, D. Sun, P. Calza, M. N. Yesibolati, P. K. Kristensen and Y. Yue, *Chem. Eng. J.*, 2024, **486**, 150207.
12 M. Long, L. Yang, C. Yang, N. A. Khan, D. An, Y. Liu and Y. Yang, *J. Membr. Sci.*, 2024, **711**, 123198.
13 J. Yu, Y. Wang, Y. He, Y. Gao, R. Hou, J. Ma, L. Zhang, X. Guo and L. Chen, *Sep. Purif. Technol.*, 2021, **276**, 119348.
14 S. Hussain, M. Salman, U. Farooq, F. Zahid, S. Yasmeen, K. M. Al-Ahmary and M. Ahmed, *Int. J. Biol. Macromol.*, 2024, **277**, 134104.
15 F. Hassanzadeh-Afruzi, G. Ranjbar, M. M. Salehi, F. Esmailzadeh and A. Maleki, *Sep. Purif. Technol.*, 2023, **306**, 122700.
16 R. Karaket, E. Detsri, A. Khattiya, P. Monvisade and A. Mathaweesansurn, *J. Chromatogr. A*, 2024, **1717**, 464668.
17 K. Lata, A. Katoch, V. Choudhary, A. Sharma, S. K. Bhatia, R. Kumar and V. S. Jaswal, *Ceram. Int.*, 2025, **51**, 54663–54681.
18 E. Choudhary, M. Samtham, R. Sharma, S. Yadav, R. Jangir and R. S. Devan, *Small*, 2025, **21**, 2410802.
19 H. Hu, M. Li, W. Xu, C. Li, A. Irfan, I. Ullah, W. ul Hasan, Q. Deng, Z. Meng and J. He, *ACS Appl. Mater. Interfaces*, 2025, **17**, 23834–23847.
20 G. S. Lee, T. Yun, H. Kim, I. H. Kim, J. Choi, S. H. Lee, H. J. Lee, H. S. Hwang, J. G. Kim and D.-w. Kim, *ACS Nano*, 2020, **14**, 11722–11732.
21 L. Meng, L. Zhou, C. Liu, H. Jia, Y. Lu, D. Ji, T. Liang, Y. Yuan, X. Zhang, Y. Zhu, Y. Jiang, P. Guan, Y. Zhou, Q. Zhang, T. Wan, M. Li, Z. Li, R. Joshi, Z. Han and D. Chu, *J. Colloid Interface Sci.*, 2024, **674**, 972–981.
22 D. Bury, M. Jakubczak, M. A. K. Purbayanto, A. Wojciechowska, D. Moszczyńska and A. M. Jastrzębska, *Small Methods*, 2023, **7**, 2201252.
23 R. Zhang, J. Liu and Y. Li, *ACS Sens.*, 2019, **4**, 2058–2064.
24 W. Jiang, X. Chen, X. Yan, J. Li, L. Xie and Y. Yu, *Colloids Surf., A*, 2024, **702**, 135098.
25 W. Guo, X. Li, T. Zhang, X. Chang and Y. An, *J. Alloys Compd.*, 2026, 188002.
26 J. Wang and X. Guo, *Chemosphere*, 2022, **309**, 136732.
27 W. Jiang, Y. Wang, Y. Wang, W. Zhou, J. Shen and Q. Liu, *Langmuir*, 2024, **40**, 27579–27591.
28 Y. Zhang, Q. Gao, S. Zhang, X. Fan, J. Qin, X. Shi and G. Zhang, *J. Colloid Interface Sci.*, 2022, **614**, 194–204.
29 P. Gao, H. Shi, T. Ma, S. Liang, Y. Xia, Z. Xu, S. Wang, C. Min and L. Liu, *ACS Appl. Mater. Interfaces*, 2021, **13**, 51028–51038.
30 Y. Zhang, K. Ruan, X. Shi, H. Qiu, Y. Pan, Y. Yan and J. Gu, *Carbon*, 2021, **175**, 271–280.
31 C. Li, Y. Luo, N. Liu, A. Zhu, Q. Liu, Z. Lin and Q. Zhang, *Adv. Funct. Mater.*, 2025, **35**, 2416490.
32 W. Zhang, T. Huang, Y. Ren, Y. Wang, R. Yu, J. Wang and Q. Tu, *Int. J. Biol. Macromol.*, 2021, **193**, 2243–2251.

33 M. Sabzevari, D. E. Cree and L. D. Wilson, *ACS Omega*, 2018, **3**, 13045–13054.
34 C. Hao, G. Li, G. Wang, W. Chen and S. Wang, *Colloids Surf., A*, 2022, **632**, 127730.
35 Z.-H. Zhang, J.-Y. Xu and X.-L. Yang, *Mater. Chem. Phys.*, 2021, **260**, 124123.
36 Y. Guo, J. Deng, J. Zhu, X. Zhou and R. Bai, *RSC Adv.*, 2016, **6**, 82523–82536.
37 N. M. Tran, Q. T. H. Ta, A. Sreedhar and J.-S. Noh, *Appl. Surf. Sci.*, 2021, **537**, 148006.
38 J. Li, L. Li, Y. Xu, J. Zhu, F. Liu, J. Shen, Z. Wang and J. Lin, *Chem. Eng. J.*, 2022, **427**, 132070.
39 M. Jiang, M. Li, C. Cui, J. Wang, Y. Cheng, Y. Wang, X. Zhang, J. Qin and M. Cao, *ACS Nano*, 2024, **18**, 7532–7545.
40 N. Jahan, H. Roy, A. H. Reaz, S. Arshi, E. Rahman, S. H. Firoz and M. S. Islam, *Case Stud. Chem. Environ. Eng.*, 2022, **6**, 100239.
41 T.-N. Kim, J. Lee, J.-H. Choi, J.-H. Ahn, E. Yang, M.-H. Hwang and K.-J. Chae, *Sep. Purif. Technol.*, 2021, **274**, 119047.
42 S. K. Tiwary, M. Singh, F. H. Likhi, S. Dabade, J. F. Douglas and A. Karim, *ACS Environ. Au*, 2024, **4**, 69–79.
43 L. P. Lingamdinne, J. R. Koduru and R. R. Karri, *J. Environ. Manage.*, 2019, **231**, 622–634.
44 Y. An, Y. Tian, H. Shen, Q. Man, S. Xiong and J. Feng, *Energy Environ. Sci.*, 2023, **16**, 4191–4250.